

Linearized spectrum correlation analysis for thermal helium beam diagnostics

Cite as: Rev. Sci. Instrum. **92**, 103501 (2021); <https://doi.org/10.1063/5.0062436>

Submitted: 05 July 2021 • Accepted: 10 September 2021 • Published Online: 04 October 2021

 T. Nishizawa,  M. Griener, R. Dux, et al.



View Online



Export Citation



CrossMark

ARTICLES YOU MAY BE INTERESTED IN

[A digital feedback system for advanced ion manipulation techniques in Penning traps](#)
Review of Scientific Instruments **92**, 103201 (2021); <https://doi.org/10.1063/5.0064369>

[“Zyflex”: Next generation plasma chamber for complex plasma research in space](#)
Review of Scientific Instruments **92**, 103505 (2021); <https://doi.org/10.1063/5.0062165>

[Cyrofluid simulation of an I-mode pedestal relaxation event](#)
Physics of Plasmas **28**, 102502 (2021); <https://doi.org/10.1063/5.0059295>



www.amscins.com

3D IMAGING of Ions & Electrons

Perfect replacement for conventional 2D cameras

TPX3CAM READOUT			
TIME OF FLIGHT EXPERIMENT		29.05.2021	
ToA (sec)	ToT (nanosec)	Coordinates	
Time of Arrival	Time over Threshold	X	Y
1.134267353184	425	144	140
1.134267353162	875	57	234
1.134267353137	875	235	149
1.134267353120	125	178	140
1.134267353111	975	5	130



Linearized spectrum correlation analysis for thermal helium beam diagnostics

Cite as: Rev. Sci. Instrum. 92, 103501 (2021); doi: 10.1063/5.0062436

Submitted: 5 July 2021 • Accepted: 10 September 2021 •

Published Online: 4 October 2021



View Online



Export Citation



CrossMark

T. Nishizawa,^{1,a)} M. Griener,¹ R. Dux,¹ G. Grenfell,¹ D. Wendler,^{1,2} S. Kado,³ P. Manz,^{1,4} M. Cavedon,¹ and ASDEX Upgrade team^{b)}

AFFILIATIONS

¹Max-Planck-Institut für Plasmaphysik, Boltzmannstr. 2, 85748 Garching, Germany

²Physik-Department E28, Technische Universität München, James-Franck-Str. 1, 85748 Garching, Germany

³Institute of Advanced Energy, Kyoto University, Uji, Kyoto 611-0011, Japan

⁴Universität Greifswald, Felix-Hausdorff-Str. 6, 17489 Greifswald, Germany

^{a)}Author to whom correspondence should be addressed: takashi.nishizawa@ipp.mpg.de

^{b)}See Meyer et al., Nucl. Fusion 59, 112014 (2019) for ASDEX Upgrade team.

ABSTRACT

We introduce a new correlation analysis technique for thermal helium beam (THB) diagnostics. Instead of directly evaluating line ratios from fluctuating time series, we apply arithmetic operations to all available He I lines and construct time series with desired dependencies on the plasma parameters. By cross-correlating those quantities and by evaluating ensemble averages, uncorrelated noise contributions can be removed. Through the synthetic data analysis, we demonstrate that the proposed analysis technique is capable of providing the power spectral densities of meaningful plasma parameters, such as the electron density and the electron temperature, even under low-photon-count conditions. In addition, we have applied this analysis technique to the experimental THB data obtained at the ASDEX Upgrade tokamak and successfully resolved the electron density and temperature fluctuations up to 90 kHz in a reactor relevant high power scenario.

© 2021 Author(s). All article content, except where otherwise noted, is licensed under a Creative Commons Attribution (CC BY) license (<http://creativecommons.org/licenses/by/4.0/>). <https://doi.org/10.1063/5.0062436>

I. INTRODUCTION

A thermal helium beam (THB) diagnostic is capable of measuring the electron density n_e and the electron temperature T_e in the scrape-off layer (SOL) and the confined region near the last closed flux surface (LCFS) in hot magnetized plasmas.^{1–4} In this diagnostic technique, a neutral helium gas is injected into the plasma, and the active emissions of multiple He I lines are observed. Generally, the ratio of a triplet to a singlet He I line is more sensitive to T_e than to n_e , while the ratio of the same spin state lines has a stronger dependence on n_e than on T_e . Thus, local measurements of n_e and T_e can be made by evaluating properly chosen line ratios.⁵ Unfortunately, some of these lines often have weak emission intensities, which necessitate time averaging of data in order to robustly evaluate n_e and T_e , resulting in reduced time resolution. In principle, the maximum achievable time resolution in the THB is set by the atomic relaxation time,⁶ provided that the optical system has an arbitrary

high throughput and photon-detection efficiency. However, practically, observable light intensities limit the time resolution under numerous circumstances, e.g., when the region near the LCFS is measured.

A diagnostic technique that is similar to the THB but more often used for fast measurements is gas puff imaging (GPI),^{7,8} which observes the two-dimensional profile of a single line intensity. Since brightness is one of the main considerations in selecting a line for GPI, a sufficient amount of light can be collected relatively easily within a short time interval. While GPI is able to resolve fast time scale fluctuations up to several hundred kHz, interpreting data is not straightforward because the active line emission intensity depends on multiple parameters.⁹ Extending the time resolution of the THB and directly investigating plasma parameter fluctuations up to high frequencies relevant to turbulent transport will help understand important topics in the edge of fusion plasmas, such as power exhaust and pedestal physics.^{10–12}

Linearized spectral correlation analysis (LSCA)^{13,14} overcomes a similar issue in ion Doppler spectroscopy, whose time resolution is also typically limited by observable light intensities. The principle of LSCA is based on the ensemble average and cross correlation. In short, this procedure is given by

$$\langle d_{1,f}^* d_{2,f} \rangle = \langle |s_f|^2 \rangle, \quad (1)$$

where

$$\begin{aligned} d_{1,f} &= s_f + X_{1,f}, \\ d_{2,f} &= s_f + X_{2,f}. \end{aligned} \quad (2)$$

Here, $d_{1,f}$ and $d_{2,f}$ are frequency components of two measurable time series, which have the same signal component s_f but different noise $X_{1,f}$ and $X_{2,f}$. The triangle bracket $\langle \dots \rangle$ stands for an ensemble average. When $X_{1,f}$ and $X_{2,f}$ are independent of each other, all terms with noise contribution converge to zero. Note that an ensemble-averaged auto-power of $d_{1,f}$ is

$$\langle |d_{1,f}|^2 \rangle = \langle |s_f|^2 \rangle + \langle |X_{1,f}|^2 \rangle. \quad (3)$$

Thus, measuring $\langle |s_f|^2 \rangle$ is difficult when $\langle |X_{1,f}|^2 \rangle$ is not negligible. The most well-known application of Eqs. (1) and (2) is probably the correlation electron cyclotron emission diagnostic, which provides T_e fluctuation power spectra even when the signals are smaller than wave noise.^{15,16} LSCA is designed to extract physically meaningful frequency power spectra from signals that depend on multiple parameters in complicated fashions. The first step of LSCA is to manipulate the dependence of each parameter by performing arithmetic operations on available time series. Then, the cross-spectra, which become less sensitive to noise as the size of an ensemble increases, are calculated.

The formalism of LSCA discussed in Ref. 13 is developed specifically for ion Doppler spectroscopy. In this paper, we reformulate LSCA for the line-ratio analysis in the THB and introduce a technique to calculate the fluctuation power spectra of n_e and T_e . This paper is organized as follows: In Sec. II, we apply arithmetic operations on time series of emission intensity data and manipulate the n_e and T_e dependence. We also take into account the noise reduction in this process. The validation of the new LSCA for the THB is given in Sec. III by using synthetic data. We evaluate cross-spectra of the quantities introduced in Sec. II and compare the results with the input spectra. The application of LSCA to real experimental data is discussed in Sec. IV. Finally, we summarize the analysis procedure, validation, and results in Sec. V.

II. MANIPULATING THE ELECTRON DENSITY AND TEMPERATURE DEPENDENCIES OF TIME SERIES

In this section, we manipulate the n_e and T_e dependencies of time series and the signal-to-noise (S/N) ratios. We consider a case where the plasma is quasi-stationary, and n_e and T_e can be decomposed into equilibrium values and small fluctuations, i.e., $n_e = n_{e,0} + \tilde{n}_e$ and $T_e = T_{e,0} + \tilde{T}_e$. When the relaxation time between the spin states can be neglected, the intensity of the He I line is given by

$$I_\lambda = n_{\text{He}} n_e \text{PEC}_\lambda(n_e, T_e), \quad (4)$$

where n_{He} is the helium atom density. The subscript λ represents the wavelength of the He I line. $\text{PEC}_\lambda(n_e, T_e)$ is called the photon

emissivity coefficient, which differs for each He I line. In this paper, we use PEC_λ provided by Ref. 6. We assume that the measurements of $\lambda = 587, 667, 706,$ and 728 nm lines are available. These four He I lines are currently measured by the THB system at ASDEX Upgrade (AUG).² However, the methodology presented herein is also applicable to different combinations of He I lines, such as in Ref. 4.

First, we divide the observable He I lines in two groups A and B and construct the following quantity:

$$\begin{aligned} R_I(n_e, T_e) &\equiv \frac{\sum_{i \in B} c_i^B I_{i,0} \sum_{k \in A} c_k^A I_k(n_e, T_e)}{\sum_{j \in A} c_j^A I_{j,0} \sum_{l \in B} c_l^B I_l(n_e, T_e)} \\ &= \frac{\sum_{i \in B} c_i^B \text{PEC}_{i,0} \sum_{k \in A} c_k^A \text{PEC}_k(n_e, T_e)}{\sum_{j \in A} c_j^A \text{PEC}_{j,0} \sum_{l \in B} c_l^B \text{PEC}_l(n_e, T_e)}, \end{aligned} \quad (5)$$

where c_x^A and c_x^B are arbitrary coefficients we can freely choose. The subscript \dots_0 indicates that the function is evaluated at $n_e = n_{e,0}$ and $T_e = T_{e,0}$, e.g., $I_{\lambda,0} \equiv I_\lambda(n_{e,0}, T_{e,0})$. Note that R_I depends only on n_e and T_e , and the contribution from n_{He} , which may hamper the n_e and T_e fluctuation measurements, is removed.

Next, we Taylor-expand R_I around $n_{e,0}$ and $T_{e,0}$ as follows:

$$R_I \approx 1 + \alpha_{n_e} \frac{\tilde{n}_e}{n_{e,0}} + \beta_{T_e} \frac{\tilde{T}_e}{T_{e,0}}, \quad (6)$$

where

$$\begin{aligned} \alpha_{n_e} &= \frac{n_{e,0}}{\sum_{j \in A} c_j^A \text{PEC}_{j,0}} \sum_{k \in A} c_k^A \left. \frac{\partial \text{PEC}_k}{\partial n_e} \right|_0 \\ &\quad - \frac{n_{e,0}}{\sum_{i \in B} c_i^B \text{PEC}_{i,0}} \sum_{l \in B} c_l^B \left. \frac{\partial \text{PEC}_l}{\partial n_e} \right|_0, \end{aligned} \quad (7)$$

$$\begin{aligned} \beta_{T_e} &= \frac{T_{e,0}}{\sum_{j \in A} c_j^A \text{PEC}_{j,0}} \sum_{k \in A} c_k^A \left. \frac{\partial \text{PEC}_k}{\partial T_e} \right|_0 \\ &\quad - \frac{T_{e,0}}{\sum_{i \in B} c_i^B \text{PEC}_{i,0}} \sum_{l \in B} c_l^B \left. \frac{\partial \text{PEC}_l}{\partial T_e} \right|_0. \end{aligned} \quad (8)$$

By adjusting the elements of A and B , c_x^A and c_x^B , the n_e and T_e dependence of R_I can be controlled. To illustrate this, we consider a case where $n_{e,0} = 7 \cdot 10^{18} \text{ m}^{-3}$ and $T_{e,0} = 50 \text{ eV}$ and evaluate

$$R_I^{(1)} = \frac{(I_{706,0} + 1.247 \cdot I_{728,0})(1.247 \cdot I_{587} + 2.441 \cdot I_{667})}{(1.247 \cdot I_{587,0} + 2.441 \cdot I_{667,0})(I_{706} + 1.247 \cdot I_{728})}, \quad (9)$$

$$R_I^{(2)} = \frac{(2.711 \cdot I_{667,0} + I_{706,0} + 44.27 \cdot I_{728,0}) \cdot I_{587}}{I_{587,0} \cdot (2.711 \cdot I_{667} + I_{706} + 44.27 \cdot I_{728})}, \quad (10)$$

and

$$R_I^{(3)} = \frac{(99.69 \cdot I_{587,0} + 180.1 \cdot I_{706,0} + I_{728,0}) \cdot I_{667}}{I_{667,0} \cdot (99.69 \cdot I_{587} + 180.1 \cdot I_{706} + I_{728})}. \quad (11)$$

Table I shows α_{n_e} and β_{T_e} for each R_I , while Fig. 1 shows R_I s as functions of n_e and T_e . When making A and B and choosing c_x^A and c_x^B for $R_I^{(1)}$, we maximized $|\alpha_{n_e}|$ while keeping $|\beta_{T_e}|$ sufficiently small with respect to $|\alpha_{n_e}|$. As a result, the contour plot of $R_I^{(1)}$ shown in

TABLE I. Coefficients of n_e and T_e fluctuations for R_I given by Eqs. (9)–(11).

	α_{n_e}	β_{T_e}
$R_I^{(1)}$	3.44×10^{-1}	-2.55×10^{-10}
$R_I^{(2)}$	1.43×10^{-10}	-8.91×10^{-1}
$R_I^{(3)}$	4.47×10^{-1}	9.07×10^{-1}

Fig. 1 has a small dependence on T_e near $n_{e,0} (= 7 \cdot 10^{18} \text{ m}^{-3})$ and $T_{e,0} (= 50 \text{ eV})$. On the other hand, in the case of $R_I^{(2)}$, we increased the sensitivity to T_e under the condition that $|\alpha_{n_e}|$ is smaller than $|\beta_{T_e}|$ by many orders of magnitude. Figures 1(a) and 1(b) show that $R_I^{(1)}$ and $R_I^{(2)}$ can be treated as functions of only n_e and T_e , respectively, near $n_{e,0}$ and $T_{e,0}$. As for $R_I^{(3)}$, we selected A, B, c_x^A , and c_x^B that lead to a high $|\alpha_{n_e} + \beta_{T_e}|$.

There are multiple combinations of A, B, c_x^A , and c_x^B that cancel the n_e or T_e dependence. In order to determine the combination that is most useful for measurements, we estimate the S/N ratio of R_I . Fast spectroscopic measurements typically employ photosensors with an internal signal amplification mechanism, such as avalanche photodiodes,^{17,18} photomultiplier tubes,^{2,19} and silicon photomultipliers.⁴ Photon noise is usually dominant over other noise sources for those sensors when properly designed electronics are used. For this reason, we evaluate the photon noise. We introduce a coefficient G that converts the light intensity into photon counts. Since the Poisson process describes the photon counting statistics, the photon noise for the signal GI_λ is $\sqrt{GI_\lambda}$. While each spectral channel can have different G in reality, we assume that G is the same for all channels for simplicity. The following discussion can be easily modified for the case where G is different for each channel. Considering the error propagation, the photon noise for $\sum_{k \in A} c_k^A I_k / \sum_{j \in A} c_j^A I_{j,0}$ is

$$\frac{\sqrt{\sum_{k \in A} (c_k^A)^2 GI_k}}{\sum_{j \in A} c_j^A GI_{j,0}}. \quad (12)$$

We can similarly define the photon noise for $\sum_{l \in B} c_l^B I_l / \sum_{i \in B} c_i^B I_{i,0}$. Again, considering the error propagation, the photon noise for R_I

is given by

$$\begin{aligned} & \sqrt{\frac{\sum_{k \in A} (c_k^A)^2 GI_k}{\left(\sum_{j \in A} c_j^A GI_{j,0}\right)^2} + \frac{\sum_{l \in B} (c_l^B)^2 GI_l}{\left(\sum_{i \in B} c_i^B GI_{i,0}\right)^2}} \\ &= \frac{1}{\sqrt{G n_{\text{He}} n_e}} \sqrt{\frac{\sum_{k \in A} (c_k^A)^2 \text{PEC}_k}{\left(\sum_{j \in A} c_j^A \text{PEC}_{j,0}\right)^2} + \frac{\sum_{l \in B} (c_l^B)^2 \text{PEC}_l}{\left(\sum_{i \in B} c_i^B \text{PEC}_{i,0}\right)^2}}. \end{aligned} \quad (13)$$

Since $1/\sqrt{G n_{\text{He}} n_e}$ is independent of A, B, c_x^A , and c_x^B , we use

$$y \equiv \sqrt{\frac{\sum_{k \in A} (c_k^A)^2 \text{PEC}_k}{\left(\sum_{j \in A} c_j^A \text{PEC}_{j,0}\right)^2} + \frac{\sum_{l \in B} (c_l^B)^2 \text{PEC}_l}{\left(\sum_{i \in B} c_i^B \text{PEC}_{i,0}\right)^2}} \quad (14)$$

at $n_e = n_{e,0}$ and $T_e = T_{e,0}$ for noise estimation.

When determining $R_I^{(1)}$, we tried out all possible combinations of elements in A and B and adjusted c_x^A and c_x^B in such a way that the T_e dependence of R_I is removed near $n_{e,0}$ and $T_{e,0}$. Then, we employed A, B, c_x^A , and c_x^B that lead to the highest $|\alpha_{n_e}/y|$. Similarly, the choice of A, B, c_x^A , and c_x^B for $R_I^{(2)}$ has the highest $|\beta_{T_e}/y|$ among the ones that cancel the sensitivity to T_e . Likewise, $R_I^{(3)}$ is constructed such that it provides the highest $|\alpha_{n_e} + \beta_{T_e}|/y$. Typically, the phase difference between n_e and T_e fluctuations is small in magnetized plasmas. Thus, the sensitivity to the plasma fluctuations is amplified when α_{n_e} and β_{T_e} have the same sign. As will be discussed in Sec. III, a high S/N ratio can be achieved by using $R_I^{(3)}$.

III. EXTRACTING POWER SPECTRAL DENSITIES FROM NOISY DATA

Here, we introduce and validate a technique to calculate power spectral densities and a relative phase between n_e and T_e from noisy data. In real measurements, the He I line intensities are subject to both plasma parameter fluctuations and noise. In order to compare the analysis results and true values, we generate synthetic THB data by using quantities shown in Table II. The equilibrium electron density and temperature are set to $n_{e,0} = 7 \cdot 10^{18} \text{ m}^{-3}$ and $T_{e,0} = 50 \text{ eV}$. These values are close to experimentally measured data that will be

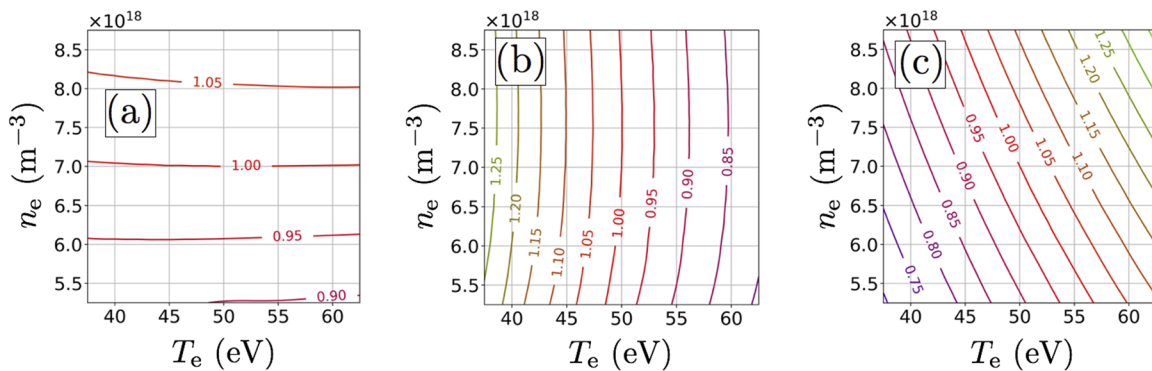


FIG. 1. (a) Contour plots of $R_I^{(1)}$ given by Eq. (9), (b) $R_I^{(2)}$ given by Eq. (10), and (c) $R_I^{(3)}$ given by Eq. (11). Each level is separated by 0.05. The n_e and T_e dependencies are optimized at $n_e = 7 \times 10^{18} \text{ m}^{-3}$ and $T_e = 50 \text{ eV}$.

TABLE II. Simulation parameters. The power spectral densities of $S_a^{1/f}$ and $S_b^{1/f}$ are inversely proportional to the frequency. The mean and the standard deviation are 0 and 1, respectively, for both $S_a^{1/f}$ and $S_b^{1/f}$. σ_x/x_0 is the standard deviation of a quantity x normalized by its mean. Note that n_{He} is set to be dimensionless for simplicity. Photon counts are set by adjusting G . Therefore, the absolute value of n_{He} does not affect the properties of synthetic data.

Quantity	Value	Units
$n_{e,0}$	7×10^{18}	m^{-3}
$T_{e,0}$	50	eV
f	50	kHz
$n_e(t)/n_{e,0}$	$1 + 0.1 \sin(2\pi ft) + 0.2S_a^{1/f}$	
$T_e(t)/T_{e,0}$	$1 + 0.1 \sin(2\pi ft - \frac{\pi}{6}) + 0.1S_b^{1/f}$	
n_{He}	$1 + 0.2S_b^{1/f}$	
$\sigma_{n_e}/n_{e,0}$	20.2	%
$\sigma_{T_e}/T_{e,0}$	13.3	%
$\sigma_{n_{\text{He}}}/n_{\text{He},0}$	20.0	%
$GI_{587}(n_{e,0}, T_{e,0})$	324.1	Counts
$GI_{667}(n_{e,0}, T_{e,0})$	96.0	Counts
$GI_{706}(n_{e,0}, T_{e,0})$	51.4	Counts
$GI_{728}(n_{e,0}, T_{e,0})$	19.4	Counts
Sampling frequency	1	MHz
FFT window	256	μs
No. of spectral samples	5000	

discussed in Sec. IV. The fluctuations of n_e and T_e are totally coherent. We add a source of fluctuations at 50 kHz, where the relative phase between n_e and T_e is $-\pi/6$. The power spectral densities of n_e and T_e given by the other source of fluctuations $S_a^{1/f}$ and $S_b^{1/f}$ are inversely proportional to the frequency. $\sigma_{n_e}/n_{e,0}$ and $\sigma_{T_e}/T_{e,0}$ are typical values for near the LCFS.²⁰ The n_{He} fluctuations, which we try to cancel in this analysis, are also modeled by a $1/f$ power spectrum. This fluctuation is incoherent with those of n_e and T_e .

We generate synthetic data for four He I lines $\lambda = 587, 667, 706,$ and 728 nm. We choose the sampling frequency of 1 MHz, which is close to that of the THB diagnostic at AUG (900 kHz). The signal amplitude at each time point is the number of photons integrated over $1 \mu\text{s}$. The line-intensity-to-photon-count conversion factor G is adjusted such that the sum of all He I line signals leads to the photon flux of around 500 counts/ μs for $n_e = n_{e,0}, T_e = T_{e,0}$, and $n_{\text{He}} = 1$. An example of the time series of GI_λ obtained through this procedure is shown in the red dotted lines in Fig. 2. Then, we add photon noise by resampling all the time points from Poisson distributions with the means equal to the original photon counts and generate synthetic He I line intensity data d_λ . Time traces of d_λ are also shown in the blue solid lines in Fig. 2.

Next, we redefine Eq. (5) using d_λ ,

$$R_d \equiv \frac{\sum_{i \in B} c_i^B \langle d_i \rangle}{\sum_{j \in A} c_j^A \langle d_j \rangle} \frac{\sum_{k \in A} c_k^A d_k}{\sum_{l \in B} c_l^B d_l}. \quad (15)$$

We Taylor-expand Eq. (15) around $n_{e,0}$ and $T_{e,0}$ in analogy with Eq. (5). Then, we consider the frequency component of R_d as follows:

$$R_{d,f} \approx \alpha_{n_e} \frac{\tilde{n}_{e,f}}{n_{e,0}} + \beta_{T_e} \frac{\tilde{T}_{e,f}}{T_{e,0}} + X_{f,1}, \quad (16)$$

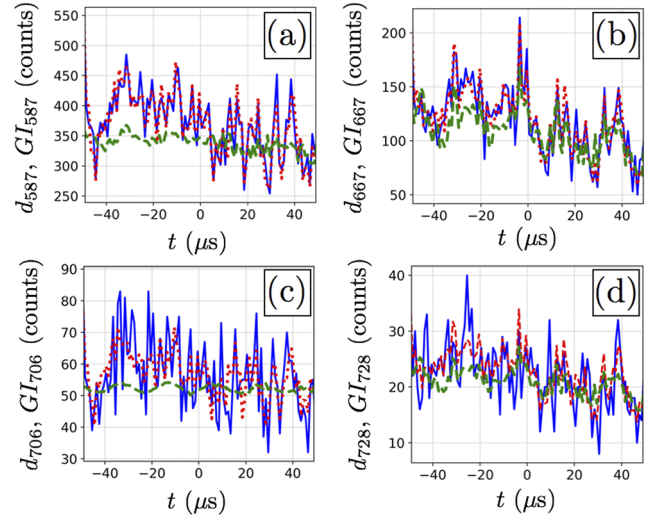


FIG. 2. Time evolution of the synthetic He I line data. (a) $\lambda = 587$ nm, (b) $\lambda = 667$ nm, (c) $\lambda = 706$ nm, and (d) $\lambda = 728$ nm. The blue solid lines show d_λ s, while the red dotted lines are GI_λ s, which are free of photon noise. The green dashed lines represent GI_λ s with $n_{\text{He}} = 1$ (constant), i.e., a case where the n_{He} fluctuations are negligible.

where $X_{f,1}$ is a noise term. α_{n_e} and β_{T_e} are given by Eqs. (7) and (8). In order to remove the noise contribution, we prepare another time series as follows, which measures the same spatial point as the first one by using a different photon detector:

$$R'_{d,f} \approx \alpha_{n_e} \frac{\tilde{n}_{e,f}}{n_{e,0}} + \beta_{T_e} \frac{\tilde{T}_{e,f}}{T_{e,0}} + X_{f,2}, \quad (17)$$

where $X_{f,2}$ is again a noise term. We assume that $X_{f,1}$ is not correlated with $X_{f,2}$, which is the case for photon noise. When we choose the same $A, B, c_x^A,$ and c_x^B as $R_I^{(1)}$, the cross-spectrum between $R_{d,f}$ and $R'_{d,f}$ becomes

$$\langle R_{d,f}^{(1)*} R_{d,f}^{(1)'} \rangle \approx \alpha_{n_e}^2 \left\langle \frac{|\tilde{n}_{e,f}|^2}{n_{e,0}^2} \right\rangle, \quad (18)$$

where the superscript $\dots^{(1)}$ indicates that it has the same $A, B, c_x^A,$ and c_x^B as $R_I^{(1)}$. We use the same notation for $R_I^{(2)}$ and $R_I^{(3)}$. Note that any term with $X_{1,f}$ and/or $X_{2,f}$ converges to zero when an ensemble average is taken. Since α_{n_e} is given by Eq. (7), in general, or by Table I for this specific case, the power spectral density of n_e can be calculated from Eq. (18). Similarly, the T_e power spectral density is given by

$$\langle R_{d,f}^{(2)*} R_{d,f}^{(2)'} \rangle \approx \beta_{T_e}^2 \left\langle \frac{|\tilde{T}_{e,f}|^2}{T_{e,0}^2} \right\rangle. \quad (19)$$

The power spectral densities of n_e and T_e obtained by Eqs. (18) and (19) are shown in Figs. 3(a) and 3(c). The input spectra and the ones calculated by auto-power of $R_{d,f}$ and $R'_{d,f}$ are also shown. The noise floors of auto-spectra are much higher than the input

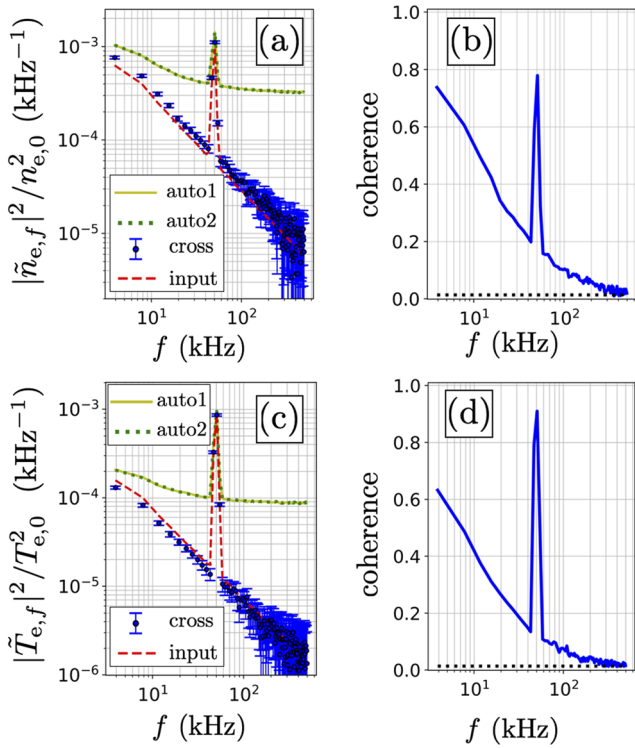


FIG. 3. Power spectral densities of n_e (a) and T_e (c). The blue points are calculated by using cross-spectra of Eqs. (18) and (19). The red dashed lines are the inputs, while the yellow solid and green dotted lines are calculated by the auto-power of $R_{d,f}$ and $R_{d,f}'$. The coherence between $R_{d,f}^{(1)*}$ and $R_{d,f}^{(1)'} R_{d,f}^{(2)}$ and $R_{d,f}^{(2)*}$ and $R_{d,f}^{(2)'} R_{d,f}^{(1)}$ are shown in (b) and (d), respectively. The black dotted lines in these plots are the statistical significance levels.

signal except 50 kHz for both n_e and T_e power spectra. However, cross-spectra remove the noise contributions and provide the power spectral densities that agree reasonably well with the input spectra. The slight overestimation of the n_e power spectrum is due

to the linear approximation since this feature remains when the photon counts are increased. The total n_e fluctuation level calculated by integrating over all frequencies is 22.3%, which is 2.1% larger than the input value shown in Table II. The T_e power spectrum is also slightly underestimated due to the linearization. Note that the range of fluctuation amplitudes within which a linear approximation holds depends on the equilibrium values of n_e and T_e .

In addition to the n_e and T_e power spectra, we calculate the cross power between the n_e and T_e fluctuations and their relative phase by using

$$\langle R_{d,f}^{(1)*} R_{d,f}^{(2)'} \rangle \approx \alpha_{n_e} \beta_{T_e} \left\langle \frac{\tilde{n}_{e,f}^* \tilde{T}_{e,f}}{n_{e,0} T_{e,0}} \right\rangle. \quad (20)$$

The results are shown in Fig. 4. The cross-spectrum reproduces the input spectrum. Furthermore, the phase lag between n_e and T_e at 50 kHz is successfully resolved in Fig. 4(b). The uncertainties of cross phase depend on coherence shown in Fig. 4(c).²¹ Above 100 kHz, the cross-phase measurements suffer large errors since the coherence level drops to near the statistical significance level.

In the end of the synthetic data analysis, we evaluate $\langle R_{d,f}^{(3)*} R_{d,f}^{(3)'} \rangle$. Neither n_e nor T_e dependence is canceled for $R_{d,f}^{(3)}$ and $R_{d,f}^{(3)'}$. This allows for a higher flexibility in choosing A , B , c_x^A , and c_x^B , and a larger reduction in photon noise becomes possible. Figure 5(a) shows the cross-spectrum between $R_{d,f}^{(3)}$ and $R_{d,f}^{(3)'}$, the corresponding input power spectrum, and auto-power spectra. The auto-spectra are closer to the input compared with Fig. 3(a) or Fig. 3(c), indicating a higher S/N ratio. Reduction in the noise contribution is also shown in Fig. 5(b). The coherence stays well above the statistical significance level up to the Nyquist frequency (=500 kHz). While $R_{d,f}^{(3)}$ and $R_{d,f}^{(3)'}$ are sensitive to both n_e and T_e , their contributions are specified by α_{n_e} and β_{T_e} , and quantitative comparisons can still be made.

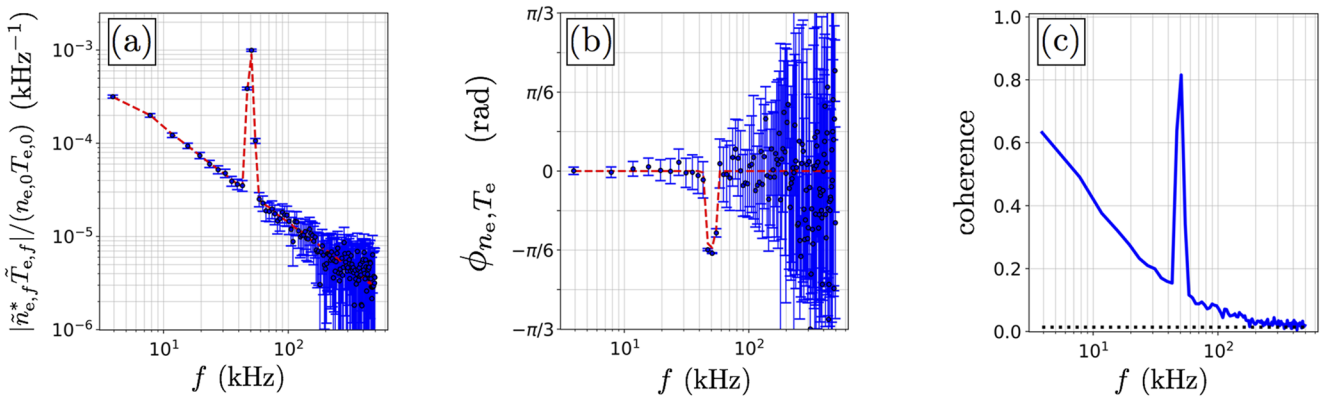


FIG. 4. (a) Cross-power spectral density between n_e and T_e fluctuations, (b) the relative phase between n_e and T_e , and (c) coherence between $R_{d,f}^{(1)*}$ and $R_{d,f}^{(2)'}$. The red dashed lines in (a) and (b) are the inputs. The black dotted line in (c) represents the statistical significance level.

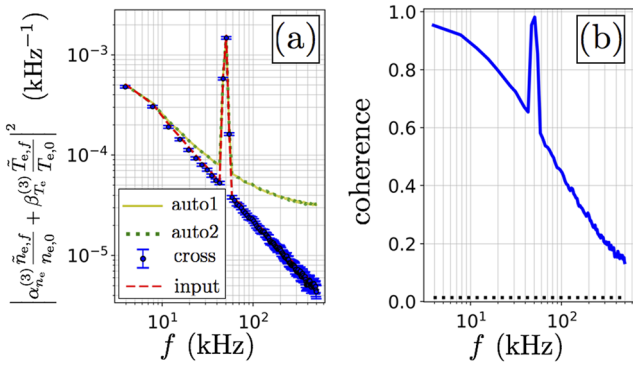


FIG. 5. (a) Power spectral densities of $\alpha_{n_e}^{(3)} \bar{n}_{e,f} / n_{e,0} + \beta_{T_e}^{(3)} \bar{T}_{e,f} / T_{e,0}$. The blue points are calculated by using a cross-spectrum. The red dashed line is the input, while the yellow solid and green dotted lines are calculated by the auto-power of $R_{d,f}^{(3)}$ and $R_{d,f}^{(3)'}.$ (b) The coherence between $R_{d,f}^{(3)}$ and $R_{d,f}^{(3)'}.$ The black dotted line is the statistical significance level.

IV. APPLICATION TO THE EXPERIMENTAL DATA

In this section, we apply LSCA to the THB data at AUG. Equation (4) is applicable only when the helium atoms travel with the equilibrated spin states. When observation points are in low density regions, care must be taken. Distances that He atoms need to travel to reach the spin state equilibrium are given in Table IV in the Appendix. We choose a radial location of $\rho_{\text{pol}} = 1.02$ in an enhanced D_α emission (EDA) H-mode plasma,¹⁰ where $n_e \sim 7 \cdot 10^{18} \text{ m}^{-3}$ and $T_e \sim 50 \text{ eV}$. As shown in Table IV, the spin states almost equilibrate within 1 mm of the traveled distance for these parameters. Therefore, Eq. (4) is expected to be a good approximation. In regard to this point, Ref. 6 reports that n_e and T_e calculated by assuming equilibrated spin states converge to the ones calculated by taking into account the time dependence of He atoms around $n_e = 2 \cdot 10^{18} \text{ m}^{-3}$. There are two spatial channels, ch. 1 and ch. 2, with the separation of $\sim 1 \text{ mm}$ at the selected radial position. We correlate those spatial channels and calculate the n_e and T_e power spectral densities.

In the THB, 667, 706, and 728 nm lines are most commonly used to determine n_e and T_e .^{3,22,23} In addition to these three lines, a 587 nm line is also measured by the AUG THB system, as already mentioned. We calculate the equilibrium n_e and T_e from the line ratios of the standard pairs, 667, 706, and 728 nm lines, and also from all four lines, 587, 667, 706, and 728 nm. When we utilize four lines, we conduct a least-square optimization by assuming the same relative uncertainties in the line intensity measurements. Note that due to a long integration time ($\sim 5 \text{ ms}$), the statistical uncertainties are negligible when determining equilibrium values. The results are shown in Table III. The differences of $n_{e,\text{three}}$ and $T_{e,\text{three}}$ between ch. 1 and ch. 2 are within the expected range of statistical or systematic errors. However, when all four lines are utilized, n_e is underestimated, and T_e is overestimated compared to the three line cases. The optical opacity of the helium gas is not responsible for this discrepancy since its escape factor was already evaluated,^{24–26} and the helium gas flow was controlled so that the photon absorption was

TABLE III. Equilibrium electron density and temperature measured by the He I line ratios at $\rho_{\text{pol}} = 1.02$ for EDA H-mode discharge No. 36 124, time 5.01–5.25 s. $n_{e,\text{three}}/T_{e,\text{three}}$ are the electron density/temperature calculated by using 667, 706, and 728 nm lines, while $n_{e,\text{four}}/T_{e,\text{four}}$ are the electron density/temperature calculated by using 587, 667, 706, and 728 nm lines.

Quantity	Ch. 1	Ch. 2
$n_{e,\text{three}}$	$8.4 \times 10^{18} \text{ m}^{-3}$	$8.0 \times 10^{19} \text{ m}^{-3}$
$n_{e,\text{four}}$	$7.3 \times 10^{18} \text{ m}^{-3}$	$6.5 \times 10^{19} \text{ m}^{-3}$
$T_{e,\text{three}}$	47.1 eV	44.5 eV
$T_{e,\text{four}}$	55.0 eV	54.0 eV

negligible for the lines of interest. Atomic modeling for plasma diagnostics is still an active field of research, and in general, modeling is not necessarily in agreement with experimental observations while significant progress has been made.^{5,27} The uncertainties of all the atomic rate coefficients and their influence onto the observed line radiation have been investigated in a new paper, which has been submitted.²⁶

Even though validating an atomic model is not within the scope of this paper, it is important to characterize how the uncertainty in the atomic model affects the n_e and T_e power spectrum measurements. To this end, we compare the power spectral densities calculated by using all four lines with the ones obtained by using only 667, 706, and 728 nm lines. Note that the formalism discussed in Secs. II and III is still applicable even when only three lines are available. For each spatial channel and for each use of He I emission lines, we determine the groups of lines A and B and coefficients c_x^A and c_x^B by following the linearization procedure at $n_{e,\text{three}}$ and $T_{e,\text{three}}$ or $n_{e,\text{four}}$ and $T_{e,\text{four}}$. Due to the differences in the equilibrium n_e and T_e values, α_{n_e} and β_{T_e} slightly differ between ch. 1 and ch. 2. When the four lines are utilized, we rescale the line intensities so that their relative intensities become the same as the atomic model calculations for the equilibrium n_e and T_e values. The corrections are less than 13%. Figure 6 shows the n_e and T_e power spectral densities. While $R_{d,f}$ and $R_{d,f}'$ are expanded and approximated by linear functions around different points, similar power spectrum densities are obtained. The peaks around 30 kHz are a quasi-coherent mode, which is usually observed near the LCFS in an EDA H-mode. When all four lines are included in the analysis, the coherence levels shown in Figs. 6(b) and 6(d) are higher, and associated statistical uncertainties are reduced. In the four line case, the coherences are above the statistical significance level up to around 90 kHz, indicating that the correlated signals originating from the n_e or T_e fluctuations are resolved below this frequency. The total n_e and T_e fluctuation levels integrated up to 90 kHz are 18.6% and 9.62%, respectively, for the three line case and 18.0% and 10.5% for the four line case. Given these fluctuation amplitudes and the equilibrium parameters in Table III, which are close to the input values in Table II, the linear approximation is not expected to introduce significant errors based on the discussion in Sec. III. Depending on the discharge scenario and the radial position, the n_e fluctuation amplitude can be larger than 20% in the SOL.²⁰ When applying LSCA, we need to keep the limit of the linear approximation in mind as well as the spin state equilibration. The applicability of LSCA can be checked by performing synthetic data analysis, such as in Sec. III.

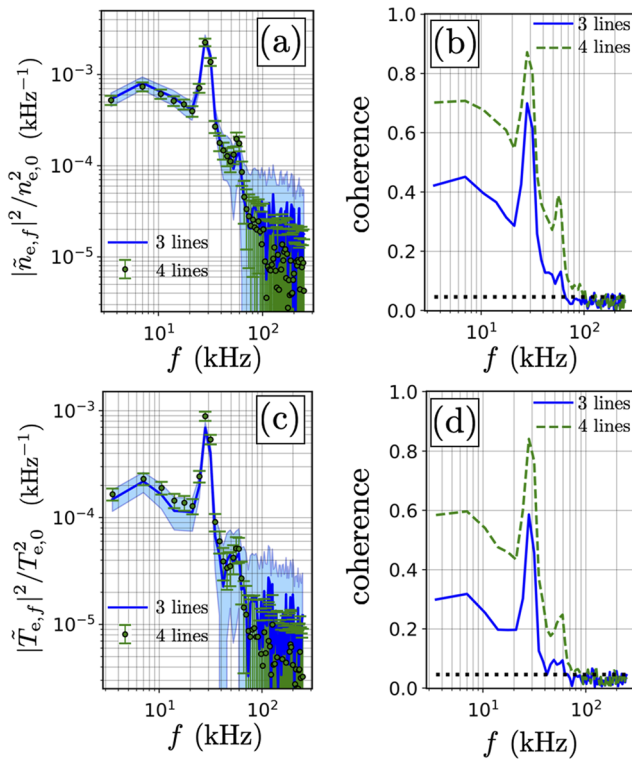


FIG. 6. Power spectral densities of n_e (a) and T_e (c) at $\rho_{\text{pol}} = 1.02$ for EDA H-mode discharge No. 36 124, time 5.01–5.25 s. The blue lines are calculated by using 667, 706, and 728 nm lines, while the green dots are calculated by using 587, 667, 706, and 728 nm lines. The blue shaded areas and the green bars account for only statistical uncertainties.²¹ The coherence of (a) and (c) are shown in (b) and (d), respectively. The black dotted lines in these plots are the statistical significance levels.

There are several other candidates of He I lines for the THB diagnostic. If those lines are measured, a further increase in coherence is expected, which helps resolve particularly high frequency ranges where the coherence level tends to be low. In addition, simultaneous measurements of more He I lines will facilitate the validation of the helium atomic model and improve the reliability of the THB.

V. SUMMARY

We have introduced linearized spectral spectrum correlation analysis (LSCA) for the thermal helium beam diagnostic. By performing arithmetic operations on He I line intensities, the contributions from neutral helium atom density fluctuations are canceled, and either the dependence on the electron density or the electron temperature is maximized or minimized. The time series with the desired parameter dependence can be expressed as a linear function of the electron density and the electron temperature around its mean values. By cross-correlating two time series constructed through this procedure and by taking ensemble averages, we can remove the noise contribution and calculate the power spectral densities of meaningful parameters.

TABLE IV. Distances required for the spin states to reach 95% of the equilibrium ratio when all atoms are initially in the ground state. The He atom velocity is set to 1.5 km/s, which is a typical value for THB diagnostics.⁶

	n_e (m^{-3})			
	4×10^{18}	7×10^{18}	1×10^{19}	
T_e (eV)	35	1.82 mm	0.84 mm	0.51 mm
	70	2.13 mm	0.97 mm	0.58 mm
	140	2.74 mm	1.24 mm	0.74 mm

The proposed analysis method is validated by using synthetic data. We have shown that the input power spectral densities of the electron temperature and the electron density can be measured even under low-photon-count conditions. When we allow the mixture of the electron density and temperature fluctuations, the signal-to-noise ratio can be improved compared with the cases where a single parameter is measured. In addition, we have applied LSCA to experimental data at ASDEX Upgrade and demonstrated that the power spectral densities of the electron density of the temperature in the scrape-off layer can be resolved up to 90 kHz. LSCA allows for quantitative comparisons between experiments and plasma edge simulations,^{28,29} which will provide insights into the edge physics in hot magnetized plasmas.

ACKNOWLEDGMENTS

The authors would like to thank Dr. J. Boedo and Dr. E. M. Hollmann for valuable discussions and Dr. J. M. Muñoz Burgos for providing the photon emissivity coefficients for He I lines. This work has been carried out within the framework of the EUROfusion Consortium and has received funding from the Euratom research and training programme 2014–2018 and 2019–2020 under Grant Agreement No. 633053. The views and opinions expressed herein do not necessarily reflect those of the European Commission.

APPENDIX: THE SPATIAL SCALE OF SPIN STATE EQUILIBRATION

This appendix includes Table IV providing the distances required for the spin states to reach 95% of the equilibrium ratio when all atoms are initially in the ground state.

DATA AVAILABILITY

The data that support the findings of this study are available from the corresponding author upon reasonable request.

REFERENCES

- B. J. Eastlund, D. Spero, M. Johnson, P. Korn, C. B. Wharton, and E. R. Wilson, *J. Appl. Phys.* **44**, 4930 (1973).
- M. Griener, E. Wolfrum, M. Cavedon, R. Dux, V. Rohde, M. Sochor, J. M. Muñoz Burgos, O. Schmitz, and U. Stroth, *Rev. Sci. Instrum.* **89**, 10D102 (2018).
- M. Agostini, P. Scarin, R. Cavazzana, L. Carraro, L. Grando, C. Taliercio, L. Franchin, and A. Tiso, *Rev. Sci. Instrum.* **86**, 123513 (2015).

- ⁴M. Agostini, P. Scarin, R. Milazzo, V. Cervaro, and R. Ghiraldelli, *Rev. Sci. Instrum.* **91**, 113503 (2020).
- ⁵M. Griener, J. M. M. Burgos, M. Cavedon, G. Birkenmeier, R. Dux, B. Kurzan, O. Schmitz, B. Sieglin, U. Stroth, E. Viezzer, and E. Wolfrum, *Plasma Phys. Controlled Fusion* **60**, 025008 (2017).
- ⁶J. M. Muñoz Burgos, O. Schmitz, S. D. Loch, and C. P. Ballance, *Phys. Plasmas* **19**, 012501 (2012).
- ⁷S. J. Zweben, J. L. Terry, D. P. Stotler, and R. J. Maqueda, *Rev. Sci. Instrum.* **88**, 041101 (2017).
- ⁸R. J. Maqueda, G. A. Wurden, D. P. Stotler, S. J. Zweben, B. LaBombard, J. L. Terry, J. L. Lowrance, V. J. Mastrocola, G. F. Renda, D. A. D'Ippolito, J. R. Myra, and N. Nishino, *Rev. Sci. Instrum.* **74**, 2020 (2003).
- ⁹I. Cziegler, P. H. Diamond, N. Fedorczak, P. Manz, G. R. Tynan, M. Xu, R. M. Churchill, A. E. Hubbard, B. Lipschultz, J. M. Sierchio, J. L. Terry, and C. Theiler, *Phys. Plasmas* **20**, 055904 (2013).
- ¹⁰L. Gil, C. Silva, T. Happel, G. Birkenmeier, G. D. Conway, L. Guimaraes, A. Kallenbach, T. Pütterich, J. Santos, P. A. Schneider, M. Schubert, E. Seliunin, A. Silva, J. Stober, U. Stroth, E. Trier, and E. Wolfrum, *Nucl. Fusion* **60**, 054003 (2020).
- ¹¹T. Kobayashi, *Nucl. Fusion* **60**, 095001 (2020).
- ¹²T. Eich, P. Manz, R. J. Goldston, P. Hennequin, P. David, M. Faitsch, B. Kurzan, B. Sieglin, and E. Wolfrum, *Nucl. Fusion* **60**, 056016 (2020).
- ¹³T. Nishizawa, M. D. Nornberg, D. J. Den Hartog, and J. S. Sarff, *Rev. Sci. Instrum.* **88**, 083513 (2017).
- ¹⁴T. Nishizawa, M. D. Nornberg, J. Boguski, D. J. Den Hartog, J. S. Sarff, Z. R. Williams, Z. A. Xing, and D. Craig, *Phys. Rev. Lett.* **121**, 165002 (2018).
- ¹⁵S. Sattler and H. J. Hartfuss, *Phys. Rev. Lett.* **72**, 653 (1994).
- ¹⁶S. J. Freethy, G. D. Conway, I. Classen, A. J. Creely, T. Happel, A. Köhn, B. Vanovac, and A. E. White, *Rev. Sci. Instrum.* **87**, 11E102 (2016).
- ¹⁷T. Kobayashi, M. Yoshinuma, and K. Ida, *Plasma Phys. Controlled Fusion* **62**, 125011 (2020).
- ¹⁸D. D. Truong, R. J. Fonck, and G. R. McKee, *Rev. Sci. Instrum.* **87**, 11E551 (2016).
- ¹⁹D. Craig, D. J. Den Hartog, D. A. Ennis, S. Gangadhara, and D. Holly, *Rev. Sci. Instrum.* **78**, 013103 (2007).
- ²⁰D. L. Rudakov, J. A. Boedo, R. A. Moyer, P. C. Stangeby, J. G. Watkins, D. G. Whyte, L. Zeng, N. H. Brooks, R. P. Doerner, T. E. Evans, M. E. Fenstermacher, M. Groth, E. M. Hollmann, S. I. Krasheninnikov, C. J. Lasnier, A. W. Leonard, M. A. Mahdavi, G. R. McKee, A. G. McLean, A. Y. Pigarov, W. R. Wampler, G. Wang, W. P. West, and C. P. C. Wong, *Nucl. Fusion* **45**, 1589 (2005).
- ²¹J. S. Bendat and A. G. Piersol, *Random Data: Analysis and Measurement Procedures*, 4th ed. (John Wiley & Sons, 1971).
- ²²O. Schmitz, I. L. Beigman, L. A. Vainshtein, B. Schweer, M. Kantor, A. Pospieszczyk, Y. Xu, M. Krychowiak, M. Lehnen, U. Samm, and B. Unterberg, *Plasma Phys. Controlled Fusion* **50**, 115004 (2008).
- ²³T. Barbui, M. Krychowiak, R. König, O. Schmitz, J. M. Muñoz Burgos, B. Schweer, and A. Terra, *Rev. Sci. Instrum.* **87**, 11E554 (2016).
- ²⁴J. M. Muñoz Burgos, M. Agostini, P. Scarin, D. P. Stotler, E. A. Unterberg, S. D. Loch, O. Schmitz, K. Tritz, and D. Stutman, *Phys. Plasmas* **23**, 053302 (2016).
- ²⁵D. Wendler, "Influence of the reabsorption on the temperature and density evaluation with the thermal helium beam diagnostic at ASDEX Upgrade," M.S. thesis, Garching: Max-Planck-Institut für Plasmaphysik, 2020; available at https://pure.mpg.de/pubman/faces/ViewItemOverviewPage.jsp?itemId=item_3241220
- ²⁶D. Wendler, R. Dux, R. Fischer, M. Griener, E. Wolfrum, G. Birkenmeier, and U. Stroth, "Collisional radiative model for the evaluation of the thermal helium beam diagnostic at ASDEX upgrade," *Plasma Phys. Controlled Fusion* (submitted) (2021).
- ²⁷Y. Iida, S. Kado, and S. Tanaka, *J. Nucl. Mater.* **438**, S1237 (2013), part of the Special Issue: Proceedings of the 20th International Conference on Plasma-Surface Interactions in Controlled Fusion Devices.
- ²⁸B. D. Scott, *Contrib. Plasma Phys.* **46**, 714 (2006).
- ²⁹W. Zholobenko, T. Body, P. Manz, A. Stegmeir, B. Zhu, M. Griener, G. D. Conway, D. Coster, and F. Jenko, *Plasma Phys. Controlled Fusion* **63**, 034001 (2021).